



 Cite this: *RSC Adv.*, 2021, **11**, 15118

# Air activation of charcoal monoliths for capacitive energy storage†

 Yu Ma, <sup>ab</sup> Hanqin Liang,<sup>a</sup> Jinwei Yin,<sup>a</sup> Dongxu Yao,<sup>a</sup> Yongfeng Xia,<sup>a</sup> Kaihui Zuo<sup>a</sup> and Yu-Ping Zeng<sup>\*a</sup>

Charcoal monoliths derived from waste wood were activated with air for the application of electrochemical capacitor electrodes and an insight was given into the activation mechanism. The mild air activation is effective and pollution-free compared to the common chemical activation using KOH *etc.* for the preparation of crack-free carbon monoliths. The activation process was controlled by altering the activation temperature and time, and their effects on the nanostructure of charcoal monoliths were studied. As the activation temperature or time increased, air eroded the defective surface of charcoal layer-by-layer, with the oxygen atoms being introduced by chemisorption and oxidation reactions and removed by dehydration and decomposition reactions. Meanwhile, micro-pores were produced. The electrode activated at 300 °C for 1 h, with a specific surface area of 567 m<sup>2</sup> g<sup>-1</sup> and a high micro-porosity of 86%, exhibited a specific capacitance of 203 F g<sup>-1</sup> and 35.5 F cm<sup>-3</sup>. Moreover, it presented a higher total capacitance of 3.6 F cm<sup>-2</sup> than most reported pellet electrodes. These findings give a reasonable picture of the air activation process and are instructive to prepare activated carbon monoliths under an oxidizing environment.

Received 19th March 2021

Accepted 15th April 2021

DOI: 10.1039/d1ra02192c

[rsc.li/rsc-advances](http://rsc.li/rsc-advances)

## 1. Introduction

The concept of sustainable development for dealing with the problem of declining fossil fuels across the world spawns ongoing research on renewable energy resources, environmentally friendly materials and green applied technologies.<sup>1–3</sup> Electrochemical energy as one form of renewable energy resource has gained more and more attention in order to relieve the increasingly intense energy and environmental crisis.<sup>4</sup> There are mainly three electrochemical energy conversion/storage technologies, including electrochemical capacitors (*i.e.*, supercapacitors or ultracapacitors), batteries and fuel cells.<sup>4</sup> Compared to the other two models, electric double layer capacitors store the energy through electrostatic adsorption charge and thus feature a high-power output and superlong cycle life, which are especially applicable to rail transportation and renewable energy production (electric power grid).<sup>5</sup> In pseudocapacitors, which are made of metal oxide or conducting polymer electrodes, a high amount of pseudocapacitance can be

introduced by faradaic electron charge-transfer with redox reactions, intercalation or electrosorption.<sup>6,7</sup> Electrode materials, the key component in the construction of capacitors, are also highly required from sustainable renewable precursors and green fabrication technology.<sup>8</sup>

Many carbon-based materials have been investigated as electrode materials, such as modified carbon materials, surface modification of carbonaceous materials, mesoporous carbon nanofibers, hierarchical nanostructured carbons with meso-macroporosity and biomass-derived carbon.<sup>9–12</sup> Biomass-derived carbon is the most used electrode materials in capacitors, Li ion batteries *etc.*, owing to the high surface area, rich surface functional groups and renewability.<sup>2,4,13</sup> The commercial carbon electrodes derived from coconut shell *etc.* are common in the form of pellets, which suffer from a limited thickness with a mass loading of <10 mg cm<sup>-2</sup> because of some introduced binders.<sup>14,15</sup> In fact, thicker electrodes possess higher total capacitance.<sup>16</sup> Ultra-thick wood carbon monoliths with hierarchically porous structure arouse increasing researchers' interest in recent years, due to their directional macro-porous channels derived from wood which provide an unobstructed pathway for charge transport.<sup>3</sup>

The carbon directly pyrolyzed from biowaste (*e.g.*, rice husk, nut shell) and wood is called biochar and charcoal, respectively. They are known as activated carbon when an activation process is applied.<sup>17</sup> Generally, two methods, including chemical activation and physical activation, are applied to prepare activated carbon materials.<sup>18</sup> Chemicals (such as potassium hydroxide,

<sup>a</sup>State Key Laboratory of High Performance Ceramics and Superfine Microstructure, Shanghai Institute of Ceramics, Chinese Academy of Sciences, Shanghai 200050, China. E-mail: yuping-zeng@mail.sic.ac.cn; my@student.sic.ac.cn; hqliang@mail.sic.ac.cn; yinjinwei@mail.sic.ac.cn; yaodongxu@mail.sic.ac.cn; yfxia@mail.sic.ac.cn; zuokh@mail.sic.ac.cn

<sup>b</sup>Center of Materials Science and Optoelectronics Engineering, University of Chinese Academy of Sciences, Beijing 100049, China

† Electronic supplementary information (ESI) available. See DOI: 10.1039/d1ra02192c



phosphoric acid, zinc chloride) introduced in the chemical activation method are harmful to the environment. In contrast, physical activation by carbon dioxide, air or steam although taking a long time is recognized in the view of little environmental impacts. The air, an available anywhere activation agent, is inevitable or introduced on purpose in the preparation of activated carbon, but with a problem of high “burn off” or a risk of combustion.<sup>19,20</sup> However, it is proposed that the pore structure and surface chemical properties of carbon materials can be improved as long as the activation temperature and time are well controlled to avoid combustion.<sup>21</sup> For example, Xuan *et al.*<sup>22</sup> enhanced electrochemical performance of the air-activated carbon spheres *via* selecting the activation temperature as 900 °C and time as 6 h in a muffle furnace. Despite that lots of works have been done to confirm the flexibility of air activation to prepare activated carbon powders,<sup>23–25</sup> few reports about production of activated carbon monoliths with air activation have been done. Even though the ultrathick activated wood-carbon is obtained by air activation at 450 °C for supercapacitor electrodes,<sup>26</sup> the detailed information about activation effects on the properties of charcoal monoliths is far from clear.

In this paper, cotton rose wood, with a unique hierarchical macro-meso-microporous structure,<sup>27</sup> was selected as the raw materials to prepare charcoal monoliths. Subsequently, a simple and mild air activation method was adopted to prepare activated carbon monoliths for the application of electrochemical capacitor electrodes. The effects of activation temperature and time on the physicochemical properties and pore structure were elaborated, in order to clarify the air activation mechanism and improve the electrochemical properties of the electrodes. Finally, the electrochemical performance is evaluated using the obtained activated carbon electrodes.

## 2. Materials and methods

### 2.1. Materials

Cotton rose wood was selected in the field, Jiangxi Province, China. Hydrochloric acid (HCl, AR) and potassium hydroxide (KOH, AR) were purchased from Sinopharm Chemical Reagent Co., Ltd., China.

### 2.2. Preparation of activated carbon monoliths

After natural drying, the wood was cut into desired thickness (2–3 mm) along radial direction and then dried overnight at 80 °C. The dried wood was pyrolyzed at 800 °C with a 5 °C min<sup>-1</sup> heating rate for 3 h under vacuum conditions with the pressure at 5–20 Pa. After cooling down, the obtained charcoal monoliths were polished to a certain size (1 cm × 1 cm × 1 mm) with a piece of metallographic abrasive paper and polished charcoal monoliths were ultrasonic cleaned for 30 min to remove attached powders. Finally, the samples were purified by 2 mol L<sup>-1</sup> HCl solution at 60 °C for 3 h and washed by distilled water until pH 7. The activation treatment for the cleaned charcoal monoliths were carried out at 300 °C, 350 °C and 400 °C for 1 h in a muffle furnace with an air environment. Above 400 °C, cracks generated in the activated carbon

monoliths resulting of severe shrinkage. To study the effect of activation time, the charcoal monoliths were activated at 300 °C for 0.5 h to 10 h in the muffle furnace.

### 2.3. Characterizations

The degree of disorder of these samples was evaluated by Raman spectrum (inVia) using a 532 nm laser. The surface functional groups were detected by Fourier transformed infrared spectroscopy (FTIR, Spotlight400). The microstructure was observed using a field emission scanning electron microscopy (FE-SEM, SU8220). The pore structure was characterized by N<sub>2</sub> adsorption/desorption method at 77 K (DEMO TriStar II 3020 V1.0). Before the test, the activated carbon monolith was grounded and passed through a 60-mesh screen. The specific surface area ( $S_{\text{BET}}$ ) indicated the Brunauer Emmett Teller (BET) surface area. Total pore volume ( $V$ ) was the N<sub>2</sub> adsorption capacity at relative pressure ( $P/P_0$ ) of 0.98 and micropore volume ( $V_{\text{micro}}$ ) was calculated using *t*-plot method. The microporosity ( $P$ ) was the ratio of ( $V_{\text{micro}}/V$ ) × 100%. Pore size ( $d$ ) was the adsorption average pore diameter ( $4 V/S_{\text{BET}}$  by BET). To analyze the elemental compositions and distinguish the chemical state of oxygen, X-ray photoelectron spectroscopy (XPS) analysis was carried out on an ESCALab250 spectrometer for both the outer and inner (etching 10 s with Ar<sup>+</sup>) surface of the activated carbon monoliths. In addition, bulk density ( $\rho$ ) was the average ratio of weight to volume of at least five electrodes. The carbon loss indicated the weight loss caused by activation of the charcoal monolith.

The electrochemical performance was evaluated on a CHI 660E electrochemical workstation (Shanghai Chenhua, China) in a three-electrode setup. The activated carbon monoliths were directly used as the working electrodes, with a mass loading ( $m$ ) of about 18 mg cm<sup>-2</sup>. A platinum plate and Hg/HgO electrode were applied as the counter and reference electrode, respectively. KOH solution (2 mol L<sup>-1</sup>) was selected as the electrolyte. The specific capacitance  $C_g$  (F g<sup>-1</sup>) was calculated according to the formula  $C_g = \frac{I \times \Delta t}{M \times \Delta V}$ , where  $I$  (A) denotes the galvanostatic discharge current in the GCD measurement,  $\Delta t$  (s) denotes the discharge time,  $M$  (g) is the mass of the working electrode, and  $\Delta V$  (V) is the potential window excluding the IR drop. The areal specific capacitance ( $C_s$ ,  $\mu\text{F cm}^{-2}$ ) was evaluated from  $C_s = \frac{100 \times C_g}{S_{\text{BET}}}$ . The total capacitance ( $C$ , F cm<sup>-2</sup>) was obtained by the formula:  $C = m \times C_g$ . The volumetric specific capacitance ( $C_v$ , F cm<sup>-3</sup>) was the result of multiplying  $C_g$  by  $\rho$ .

## 3. Results and discussion

### 3.1. The effects of activation temperature

The Raman spectra of the samples activated at 300 °C, 350 °C and 400 °C in the air, as presented in Fig. 1a (left), are typical patterns of partial graphitized carbon with D band (sp<sup>3</sup> carbon) at ~1350 cm<sup>-1</sup> and G band (sp<sup>2</sup> carbon) at ~1590 cm<sup>-1</sup>. The degree of disorder is estimated by the ratio of the intensity of D band to G band ( $I_{\text{D}}/I_{\text{G}}$ ).<sup>28</sup> As observed in Fig. 1a (right), the plot of  $I_{\text{D}}/I_{\text{G}}$  ratio *vs.* increasing activation temperature exhibits

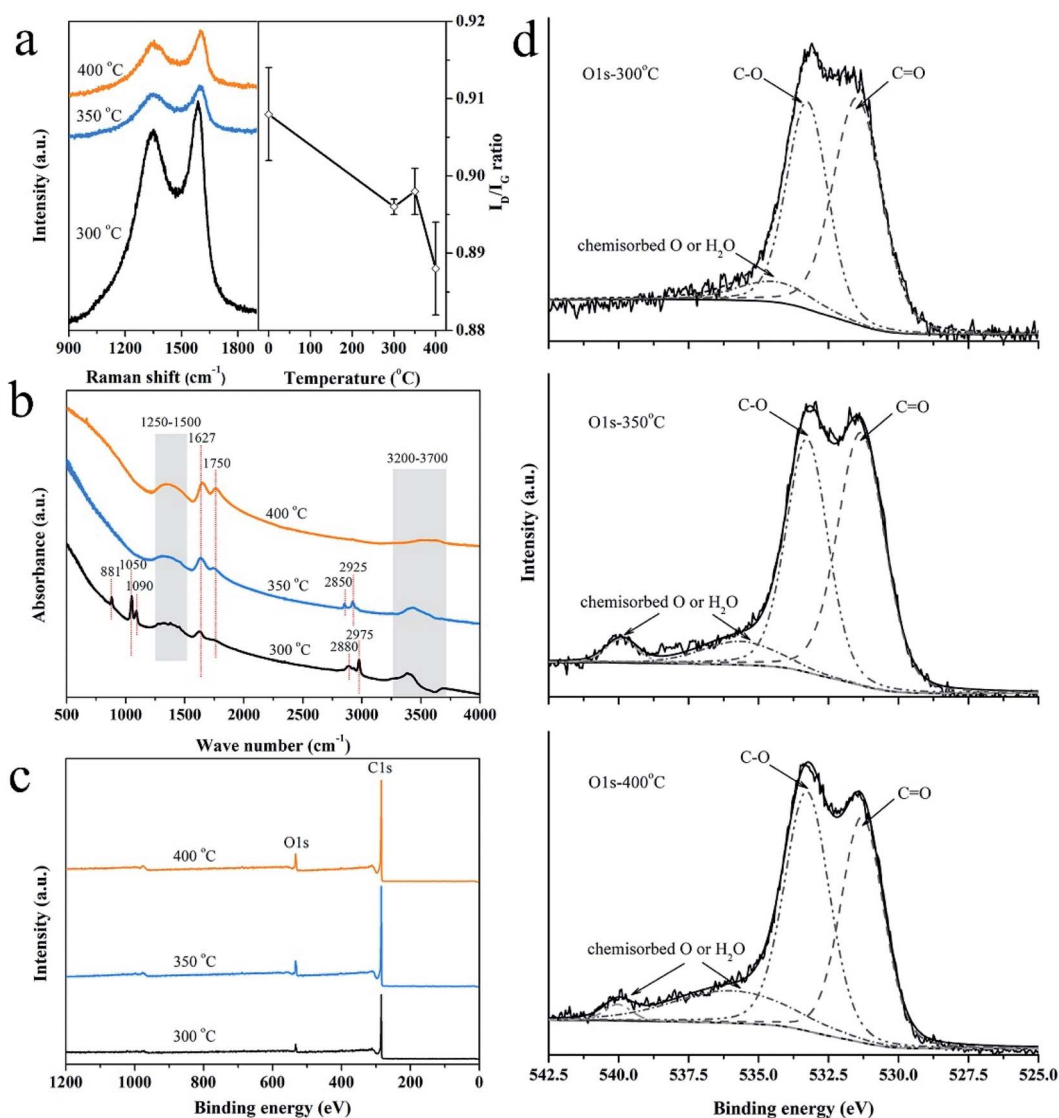


Fig. 1 (a) Raman spectra (left) and the variation of  $I_D/I_G$  ratio vs. activation temperature (right), (b) FTIR spectra, (c) survey XPS spectra and (d) deconvoluted O 1s spectra for the charcoal monoliths activated at different temperatures.

a downward trend overall. The sample at 0 °C indicates the non-activation charcoal monolith and the value was obtained from our previous work.<sup>29</sup> We proposed that improved graphitization is mainly caused by the removal of tarry gradients. In detail, the ratios drop sharply after activation at 300 °C, increase subsequently when the temperature rises up to 350 °C, and again decrease at 400 °C. It is believed to be related to the migration process of the introduced oxygen atoms during activation in air, which is further verified by FTIR analysis.

The form of introduced oxygen is mainly reflected on the surface functional groups, as revealed in Fig. 1b. For all samples, the appearance of broad band at 3200–3700  $\text{cm}^{-1}$  is contributed to the O–H bond vibration in hydroxylic groups and chemisorbed water,<sup>30</sup> the intensity of which declines with the increase of activation temperature. Moreover, alcoholic C–O bond (1050  $\text{cm}^{-1}$  and 1090  $\text{cm}^{-1}$ ) and C–H bond (881  $\text{cm}^{-1}$ ) from out of plane deformation vibrations in benzene derivatives

disappear above 300 °C.<sup>31,32</sup> By contrast, the intensity of the bonds at 1627  $\text{cm}^{-1}$  (quinone or conjugated ketone groups), 1750  $\text{cm}^{-1}$  (C=O vibration in anhydride, lactone and ketene), and the accompanied broad peak at 1500–1250  $\text{cm}^{-1}$  (C–O stretching and O–H bending modes in ether, lactone, carboxyl, phenolic structure, *etc.*) enhance.<sup>30,33,34</sup> The following reactions caused by the activation are deduced according to the above results: (1) dehydration reactions between hydroxyl groups, carboxyl groups or hydroxyl and carboxyl groups; (2) oxidation reactions that aromatic compounds (*e.g.*, benzene derivatives, alcohol organics) turn to be quinone or ketone species and further to be  $\text{CO}_2$  or CO gases.<sup>29</sup> In addition, the peaks at 2880 (or 2850)  $\text{cm}^{-1}$  and 2975 (or 2925)  $\text{cm}^{-1}$  that correspond to C–H stretching vibrations in alkane and alkene groups of aliphatic species weaken at 350 °C and disappear at 400 °C, which indicate that some small organic molecules were gradually removed.<sup>14,35</sup> In summary, the migration of oxygen atoms

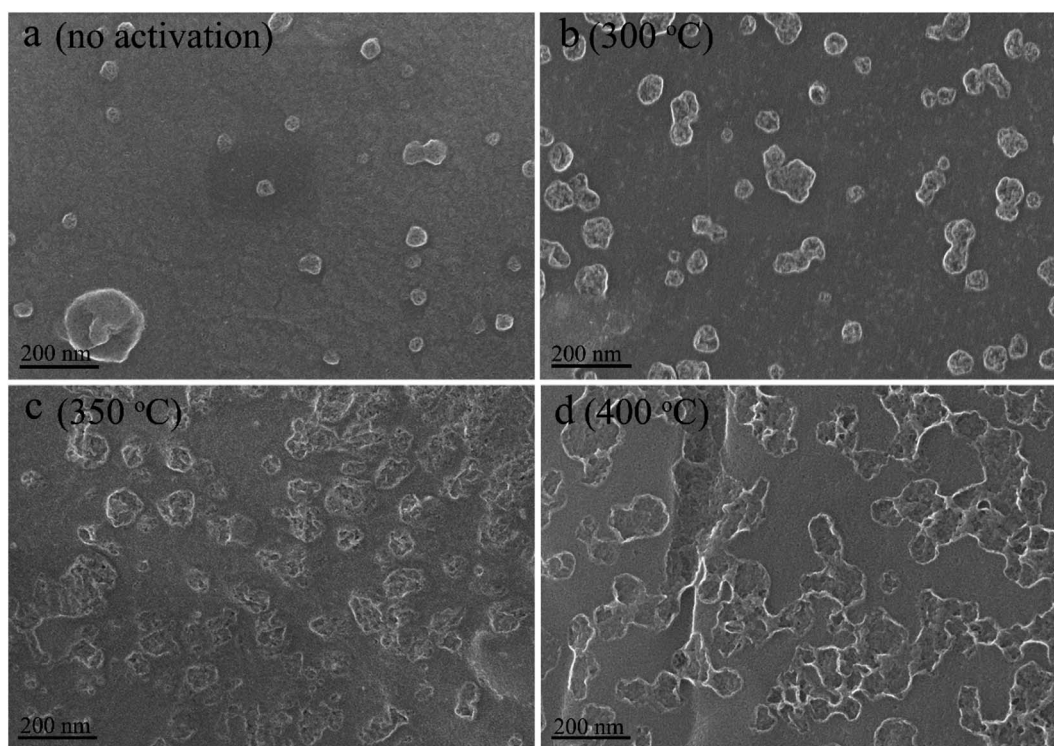
**Table 1** The contents of element contained on the surface of activated charcoal monoliths and distribution of oxygen complexes from XPS analysis

Conditions (°C-h)	Etched surface		Outer surface		Outer surface O 1s		
	C (at%)	O (at%)	C (at%)	O (at%)	C=O (%)	C-O (%)	Chemisorbed oxygen (%)
300-0.5	92.35	6.44	89.03	9.81	50.2	38.9	10.8
300-1	91.42	7.17	86.59	12	53.7	41.4	5.0
300-2	92.56	6.48	87.46	11.47	44.8	43.5	11.7
300-3	92.11	6.68	86.87	11.85	49.2	45.1	5.8
350-1	89.28	9.81	85.13	14.03	49.5	40.2	10.3
400-1	89.46	9.62	85.81	13.32	39.2	43.5	17.3

referring to the way of introduction or elimination is involved in these reactions.

Furthermore, chemical state of the introduced oxygen in the activated carbon was investigated by XPS analysis. The peaks of carbon and oxygen dominate the XPS survey spectra (Fig. 1c). Their contents of the outer and inner surface of the activated carbon monoliths are listed in Table 1. The trend of oxygen contents *vs.* activation temperature is similar to that of  $I_D/I_G$  ratios as shown in Fig. 1a (right). It is demonstrated that the degree of disorder of the activated carbon is directly related to the oxygen content. Subsequently, the O 1s spectra are deconvoluted to identify the chemical status of oxygen atoms, as shown in Fig. 1d. The peak at  $\sim 531.3$  eV indicates the existence of C=O bond in carbonyl or quinone groups and the peak at  $\sim 533.3$  eV refers to C-O bond in esters, ether, phenol or hydroxyls.<sup>30,36-38</sup> The peaks at above 534 eV are assigned to

chemisorbed oxygen (-COOH) or water molecular.<sup>30</sup> The contribution of cover area of each peak is listed in Table 1. On one hand, the content of chemisorbed O increases with the increase of activation temperature, which indicates the generation of more and more new surface. On the other hand, the contents of C=O groups decrease rapidly because high temperature promotes their decomposition to form CO<sub>2</sub> gases.<sup>39</sup> In comparison, the C-O groups change slightly because they are quite stable. In summary, chemisorbed oxygen (*e.g.*, carboxyl groups) that is the most sensitive to activation temperature is the initial form of introduced oxygen whose content changes quickly with the activation temperature. Subsequently, oxidation and dehydration reactions occur accompanying with the generation of ether and ester species as these groups are more stable than hydroxyl groups and carboxylic acid at 300-450 °C.<sup>39</sup> At last, these formed groups decompose to CO<sub>2</sub> and/or CO gases

**Fig. 2** SEM micrographs of cell surface of the charcoal monoliths activated at (a) none, (b) 300 °C, (c) 350 °C, and (d) 400 °C.



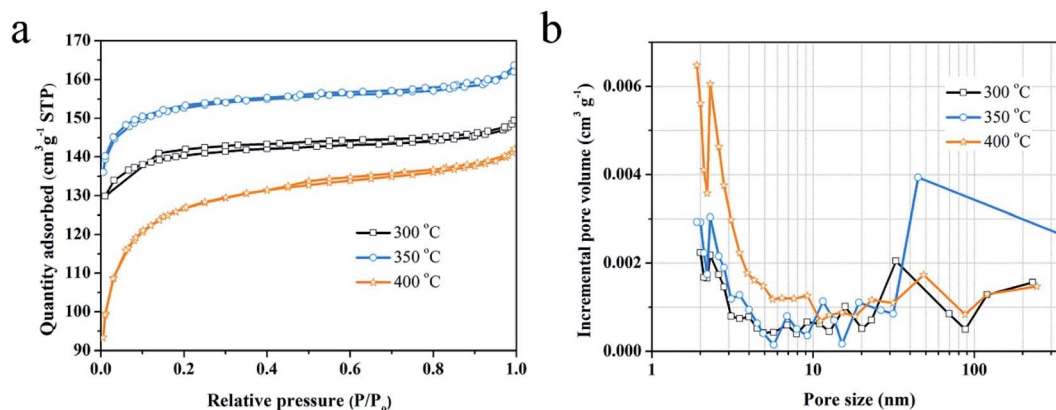


Fig. 3 (a)  $N_2$  adsorption/desorption isotherms and (b) pore size distribution for the charcoal monoliths activated at different temperatures.

and new pores generate simultaneously, which is confirmed by the variation of carbon loss from about 3 wt% both at 300 °C and 350 °C to 13 wt% at 400 °C. In addition, the enhanced  $O_2$  diffusion along the defect sites initially also promotes the formation of pores in the oxidation process.

Fig. 2 and S3† display the SEM micrographs of the channel surface at various activation temperatures and the activated carbon monolith (activated at 300 °C for 1 h), respectively. The activated carbon monoliths exhibit a directional hierarchical porous structure with a honey-combed configuration in the transverse section (Fig. S3a†) and abreast channels with many interconnected pores in the vertical section (Fig. S3b†). Fig. 2a shows the cell surface of charcoal monolith obtained from vacuum pyrolysis without activation. The bulges generate as a result of the rapid removal of volatiles from defective sites. By contrast, bulges evolve to be pits in Fig. 2b–d and these pits become larger and deeper with gradually rising activation temperature. Furthermore, much more secondary pits are observed on the surface of those initial pits, as shown in Fig. 2c and d. The  $O_2$  diffuses along the defect locations of the charcoal surface accompanying with the activation process proceeding layer by layer along the defect edge, which is consistent with the reported “reaming” effect by Xiao *et al.*<sup>40</sup> This explains why the oxygen content contained in the activated carbon increases and decreases repeatedly. The surface tends to absorb oxygen when new surface exposes and excludes oxygen through dehydration

and decomposition reactions when the chemisorbed oxygen is saturable.

The  $N_2$  adsorption/desorption isotherms and pore size distributions are shown in Fig. 3. The samples activated at 300 °C and 350 °C exhibit a type I  $N_2$  adsorption/desorption isotherms with a steep adsorption of  $N_2$  at the very low relative pressure and a weak capillary condensation at very high relative pressure (Fig. 3a), which correspond to microporous dominated structure.<sup>41</sup> The sample activated at 350 °C shows a higher adsorption capacity of  $N_2$ , possessing a specific surface area of  $601 \text{ m}^2 \text{ g}^{-1}$  and a pore volume of  $0.25 \text{ cm}^3 \text{ g}^{-1}$ , which is higher than that of the sample activated at 300 °C (Table 2). Additionally, the micro-porosity for both of them are above 80%. When the activation temperature rises up to 400 °C, the  $N_2$  adsorption/desorption isotherms turn to be type IV with a hysteresis loop at the relative pressure of above 0.4, indicating a mesoporous structure.<sup>42</sup> The specific surface area and the micro-porosity are  $469 \text{ m}^2 \text{ g}^{-1}$  and 64%, respectively. As shown in Fig. 3b, the obtained activated carbon all present a wide pore size distribution. The pore size distribution for the samples activated at 300 °C and 350 °C is alike in the mesopore range, except for a slight increase in the range of 2–3 nm for the latter. However, the quantity of macropores increase evidently for the sample activated at 350 °C. The sample activated at 400 °C features richer mesopores, especially the pores with a diameter of smaller than 10 nm, but the macropores are not salient. This demonstrates that micropores are etched to be meso-macropores and then micropores form again on the surface of the previous meso-macropores with increasing temperature, in agreement with above mentioned description about the air activation processes.

Table 2 The pore structure parameters of activated charcoal monoliths

Conditions (°C-h)	$\rho$ ( $\text{g cm}^{-3}$ )	$S_{\text{BET}}$ ( $\text{m}^2 \text{ g}^{-1}$ )	$V$ ( $\text{cm}^3 \text{ g}^{-1}$ )	$P$ (%)	$d$ (nm)
300-0	$0.182 \pm 0.005$	226	0.12	68	2.15
300-0.5	$0.180 \pm 0.001$	493	0.20	84	1.63
300-1	$0.175 \pm 0.003$	567	0.23	86	1.61
300-2	$0.180 \pm 0.004$	565	0.23	85	1.61
300-3	$0.183 \pm 0.004$	617	0.25	84	1.63
350-1	$0.171 \pm 0.001$	601	0.25	84	1.67
400-1	$0.169 \pm 0.002$	469	0.22	64	1.84

### 3.2. The effects of activation time

Raman spectra of the samples activated at 300 °C for different time are presented in Fig. 4a (left) and S1,† which display that these samples are all partial graphitized. The ratios for  $I_{\text{D}}/I_{\text{G}}$  experience a process of repeated rise and fall from 0.5 h to 10 h, but a downward trend on the whole (Fig. 4a, right). As demonstrated above, the ratio has a direct relationship with the oxygen content contained in the activated carbon. Therefore, the

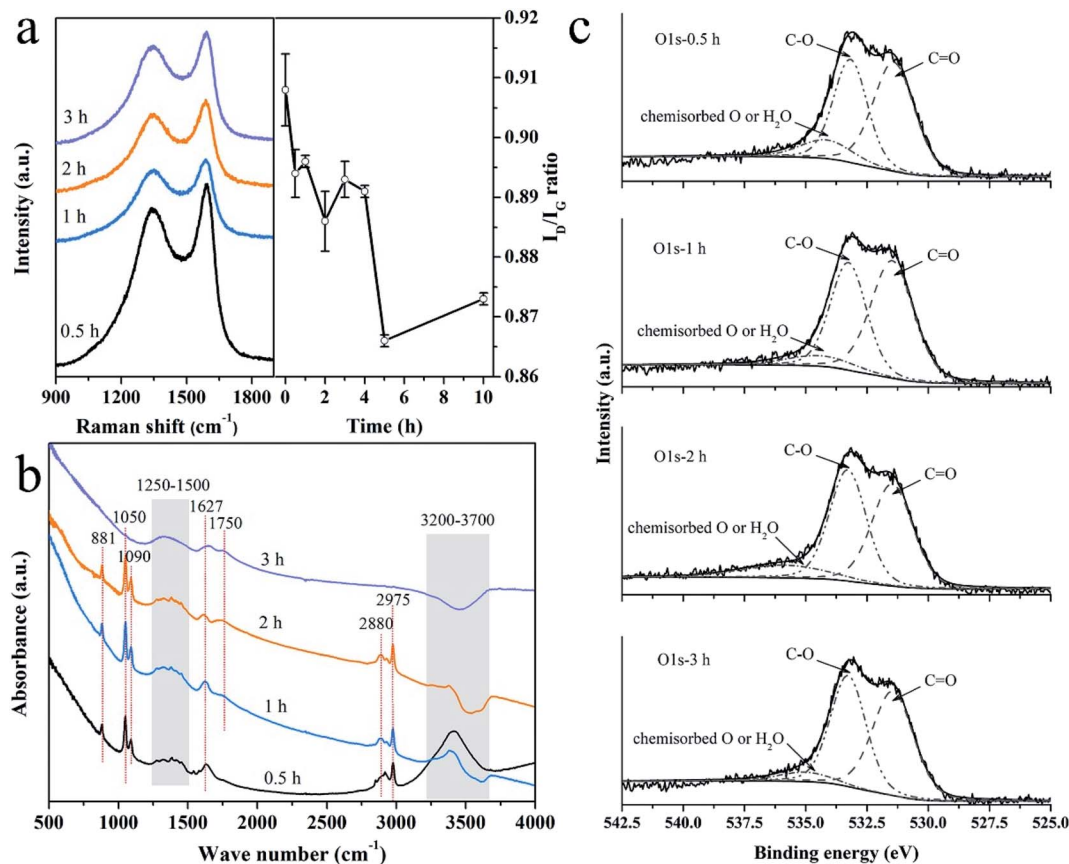


Fig. 4 (a) Raman spectra (left) and the variation of  $I_D/I_G$  ratio vs. activation time (right), (b) FTIR spectra, (c) deconvoluted O 1s spectra for the charcoal monoliths activated for different time.

activation time on the activated carbon have similar effect with activation temperature that induces a dynamic oxygen migration process.

Fig. 4b presents the FTIR spectra of the samples activated for various time. As observed, the bond intensity of hydrogen groups at 3200–3700 cm<sup>-1</sup> decreases obviously with the gradually extended activation time. In addition, those peaks at 2880 cm<sup>-1</sup>, 2975 cm<sup>-1</sup>, 1050 cm<sup>-1</sup>, 1090 cm<sup>-1</sup> and 881 cm<sup>-1</sup> disappear until for 3 h, indicating that the organic molecules, adhering to carbon skeleton, are removed or oxidized completely. The peak at 1750 cm<sup>-1</sup> (C=O vibration in lactone *etc.*) generates after activation for 1 h and continuously enhances as the activation time is prolonged to 3 h. By contrast, the bond at 1627 cm<sup>-1</sup> derived from quinone species always exists, denoting that the dehydration reaction between carboxyl groups is, to some extent, more difficult to occur than the oxidation reactions.

The XPS analyzing results of the carbon and oxygen contents contained in the activated carbon monoliths are listed in Fig. S2† and Table 1. As expected, changes of oxygen content are consistent with the changes of  $I_D/I_G$  ratio. It is confirmed that oxygen content directly influences the degree of disorder of the activated carbon. Further, high-resolution O 1s XPS spectra are shown in Fig. 4c and the contents of various forms of oxygen are listed in Table 1. The results indicate that the introduced oxygen in the charcoal exists in the forms of C–O, C=O and

chemisorbed oxygen. The content of chemisorbed oxygen proceeds a periodical process of falling and rising, accompanying with an opposite trend for the contents of C=O. Therefore, it is proposed that the chemisorbed oxygen is expected to turn to be carbonyl containing groups (C=O) *via* dehydration reaction. That is, the charcoal surface mainly adsorbed oxygen from the air in a short activation time of 0.5 h, subsequently dehydration reaction between surface functional groups dominated with the activation time extending to 1.0 h (Fig. 4c). Once these unstable C=O groups decompose to CO<sub>2</sub>, new active surface is exposed and chemisorbed reaction to oxygen starts again.

Fig. 5 exhibits the cell surface morphology of activated carbon monoliths with different activation time. Increasing activation time from 0.5 h to 3 h, the number of pits increases with the average size scaling up from 20 μm to 50 μm. Compared with the surface morphologies in Fig. 2, the edges of pits become smoother, indicative of milder activation effect than that of activation temperature. For instance, the pits on the cell surface of the samples activated for a long time (4–10 h, Fig. S4†) is being deeper and larger, similar to the surface morphology of the sample activated at 350 °C (Fig. 2c). Moreover, TEM micrographs confirm that much more micro-mesopores are created on the carbon sheet of activated carbon (Fig. 5e) than the non-activation one (Fig. 5f), as shown in the marking areas by yellow lines.

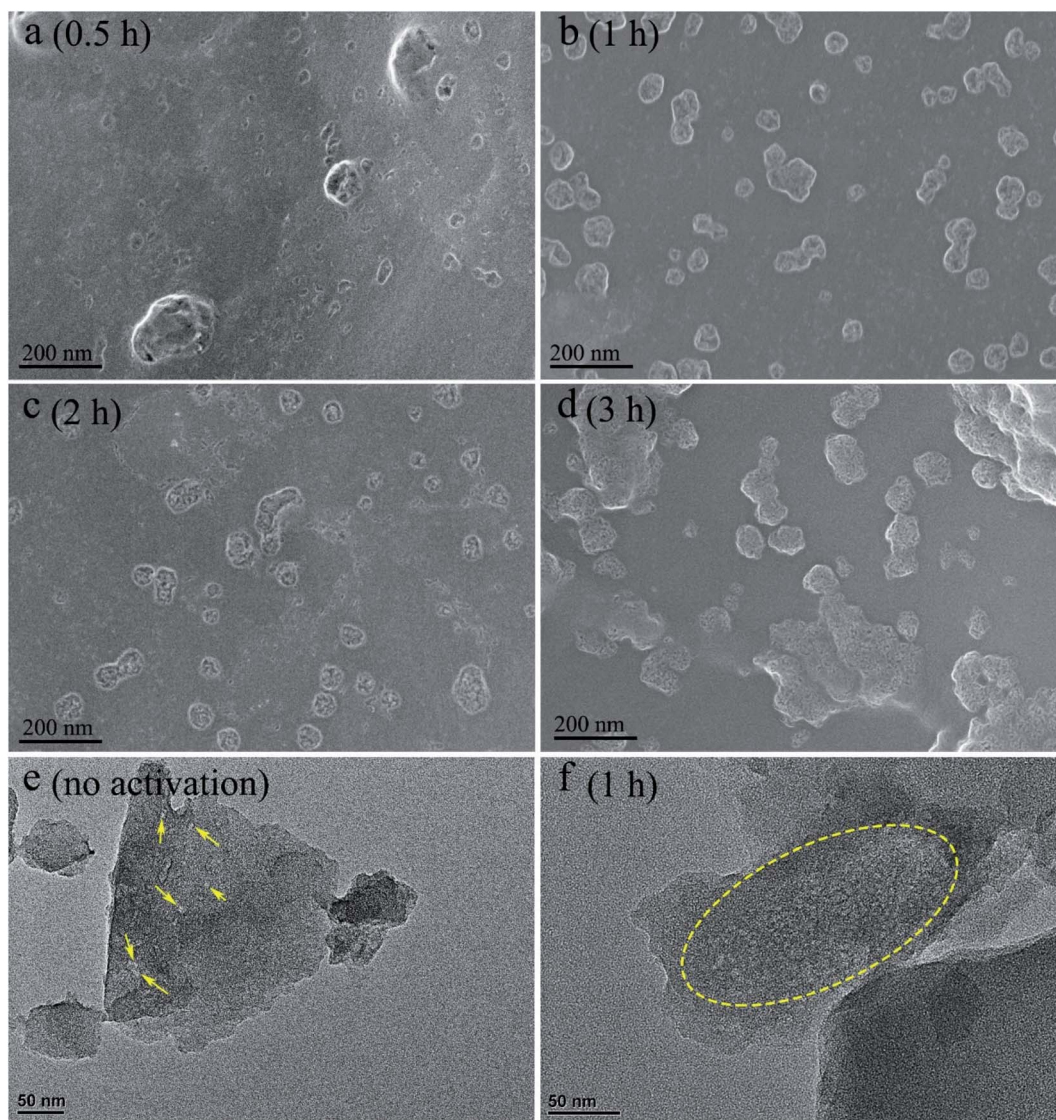


Fig. 5 SEM micrographs of cell surface for the charcoal monoliths activated for (a) 0.5 h, (b) 1 h, (c) 2 h and (d) 3 h; TEM micrographs of carbon sheets activated for (e) none, (f) 1 h.

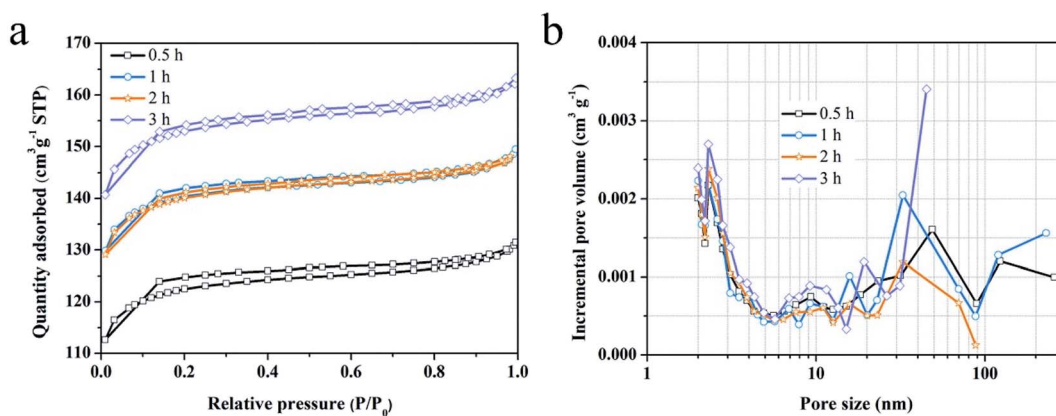


Fig. 6 (a)  $\text{N}_2$  adsorption/desorption isotherms and (b) pore size distribution for the charcoal monoliths activated for 0.5 to 3 h.



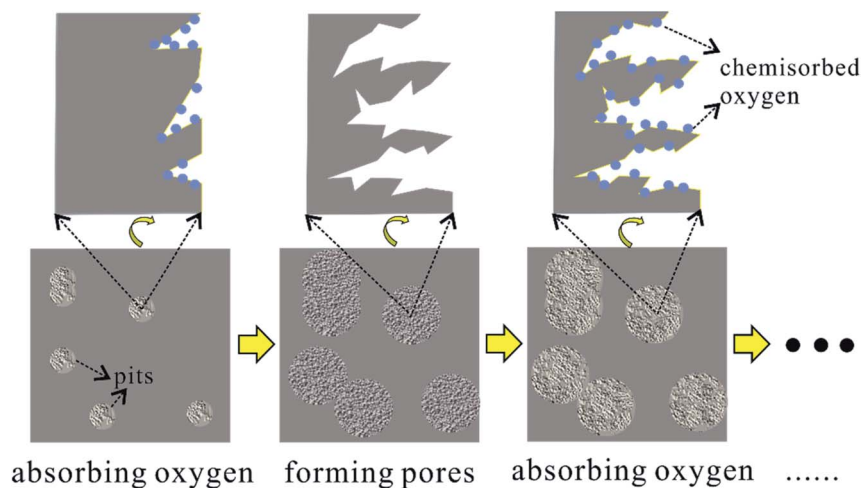


Fig. 7 Schematic diagram of the layer-by-layer pore forming mechanism of air activation.

Type I  $N_2$  adsorption/desorption loop are observed for the samples activated for different time, as shown in Fig. 6. Air activation promotes the specific surface area of the original charcoal from  $226 \text{ m}^2 \text{ g}^{-1}$  to  $617 \text{ m}^2 \text{ g}^{-1}$  after activation for 0.5 h to 3 h, and upgrades the pore volume from  $0.12 \text{ cm}^3 \text{ g}^{-1}$  to  $0.25 \text{ cm}^3 \text{ g}^{-1}$  (Table 2). In comparison, the micro-porosity reaches the maximum value of 86% for 1 h, which is related to the variation of pore size. With the increasing of activation time,

more and more micropores generate on the surface of pits and then these micropores are enlarged to be meso-macropores, as the description for SEM images (Fig. 5a–d). Notably, there is merely change for pore structure parameters between the samples activated for 1 h and for 2 h. This indicates that the reaction of chemisorbing oxygen from the air dominate this period, with few pores being generated. Nevertheless, this phenomenon does not occur with the increase of activation

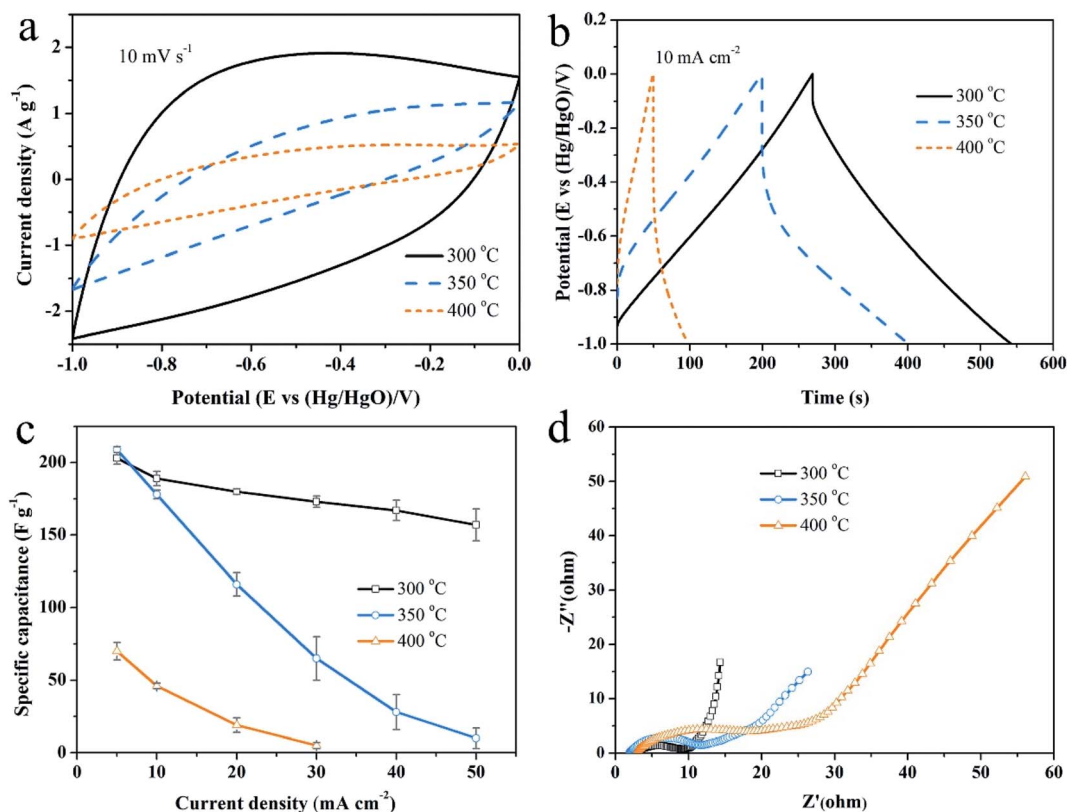


Fig. 8 The effects of activation temperature on the electrochemical performance. (a) CV curves at  $10 \text{ mV s}^{-1}$ , (b) GCD plots at  $10 \text{ mA cm}^{-2}$ , (c) EIS spectra, (d) comparison of specific capacitances.

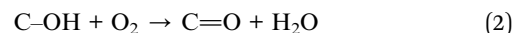


temperature whose effects are so drastic that the pore structure varies fast even in the process of absorbing oxygen. Additionally, altering the activation time, the bulk density of activated carbon monolith does not change much, but decreases obviously with the increasing of activation temperature. It is also suggestive of the prominent role of activation temperature.

### 3.3. Mechanism of activation reactions and pore formation

Based on the results mentioned above, there are four types of reactions taking place during the air activation process, including absorbing reactions, oxidation reactions, dehydration

reactions and decomposition reactions. The representative reactions are shown in formulas (1)–(4), respectively.



In general, the oxygen in air is introduced by formulas (1) and (2) and removed by formulas (3) and (4). Meanwhile, pores

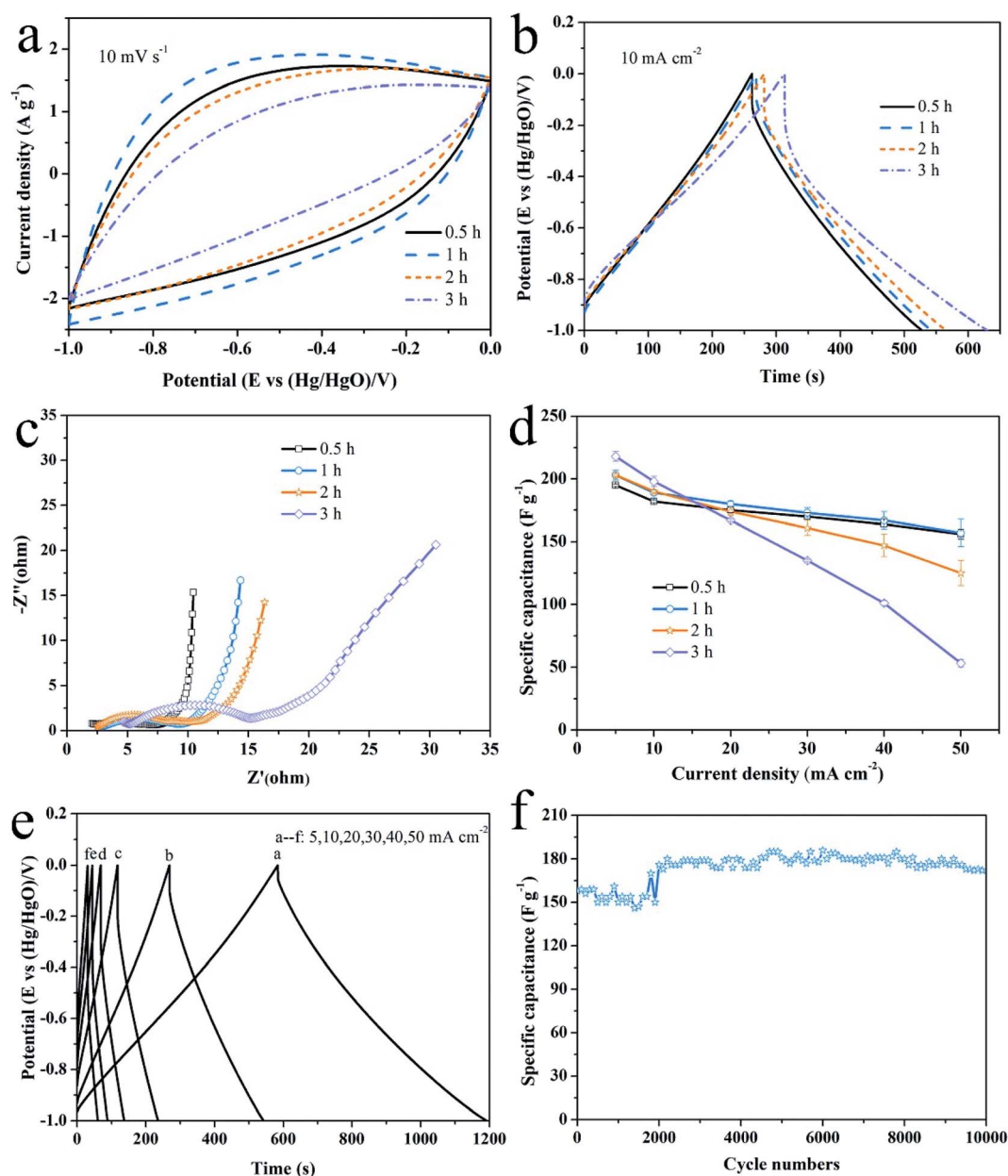


Fig. 9 The effects of activation time on the electrochemical performance. (a) CV curves at  $10 \text{ mV s}^{-1}$ , (b) GCD plots at  $10 \text{ mA cm}^{-2}$ , (c) EIS spectra, (d) comparison of specific capacitances. (e) GCD plots at various current densities and (f) cycling test at  $50 \text{ mA cm}^{-2}$  for 10 000 cycles for the electrode activated for 1 h.

Table 3 The comparison of various capacitance for activated carbon electrodes in pellet or monolith form in a three-electrode system

Raw materials	Activation agents	$C_g$ ( $F g^{-1}$ )	$C_s$ ( $\mu F cm^{-2}$ )	$C_v$ ( $F cm^{-3}$ )	$C$ ( $F cm^{-2}$ )	Test conditions	$m$ ( $mg cm^{-2}$ )	Form	Ref.
Bamboo	$K_2FeO_4$	222	12.8	—	0.7	6 M KOH $0.5 A g^{-1}$	3	Pellet	47
Cornstalk	$K_2C_2O_4$	337	17.6	—	0.1	1 M $H_2SO_4$ $1 A g^{-1}$	0.28	Pellet	48
Corn husk	KOH	356	41.1	—	0.7	6 M KOH $1 A g^{-1}$	2	Pellet	36
Celtuce leaves	KOH	421	12.4	—	3.4	2 M KOH $0.5 A g^{-1}$	8	Pellet	49
Wood tar	KOH	338.5	17.8	—	1.0	6 M KOH $1 A g^{-1}$	3	Pellet	50
Mushroom	$H_3PO_4/KOH$	306	10.2	—	0.6	6 M KOH $1 A g^{-1}$	2	Pellet	43
Pomelo peel	KOH	230	13.3	—	—	2 M KOH $1 A g^{-1}$	—	Pellet	51
Cornstalk	$K_4[Fe(CN)_6]$	213	27.0	—	—	6 M KOH $1 A g^{-1}$	3.75	Pellet	52
Tealeaves	KOH	330	11.6	—	2.6	2 M KOH $1 A g^{-1}$	8	Pellet	53
Coconut shell	$ZnCl_2/FeCl_3$	268	14.3	—	0.1	6 M KOH $1 A g^{-1}$	—	Pellet	54
Poplar wood	$HNO_3$	235	56.5	35.3	3.5	2 M KOH $5 mA cm^{-2}$	15	Monolith	55
Cedar wood	$HNO_3$	115	36.3	—	1.4	5 M $H_2SO_4$ $0.5 A g^{-1}$	—	Monolith	56
Chinese fir	$CO_2/KOH/HNO_3$	285.6	40.6	—	—	1 M $Na_2SO_4$ $10 mA cm^{-2}$	—	Monolith	57
Lignin	—	208.4	26.0	97.1	3	6 M KOH $0.1A g^{-1}$	14.4	Monolith	45
Phenolic resol	N-doped	147.9	—	21.5	—	6 M KOH $1 A g^{-1}$	—	Monolith	58
Resorcinol-formaldehyde	—	159.6	—	28.7	—	6 M KOH $0.2 A g^{-1}$	—	Monolith	59
Cotton rose-1 h	Air	203	35.8	35.5	3.6	2 M KOH $5 mA cm^{-2}$	17.5	Monolith	This work

generate on the surface of charcoal. Here, a layer-by-layer model is proposed for the pore forming process, as illustrated in Fig. 7. The defect locations on the surface of charcoal tend to adsorb oxygen at the elevated temperatures. Subsequently, enhanced  $O_2$  diffusion and reactions between oxygen related surface functional groups erode the surface carbon to generate pores. When fresh surface is exposed, the process of chemisorbing oxygen dominates again. Furthermore, this layer-by-layer pore forming mechanism is expected to explain the pore forming process by any other oxidizing gases (*e.g.*,  $CO_2$ , steam).

### 3.4. Evaluation of electrochemical performance

As shown in Fig. 8, the effects of activation temperature on the electrochemical performance were studied by CV, GCD and EIS measurements. The area covered by CV loop denotes the capacitive ability of an electrode. Judging from Fig. 8a, the capacitive performance of electrode gets worse with the increasing of activation temperature. Accordingly, the discharge time of GCD curve (Fig. 8b) becomes shorter at the same current density. Moreover, the IR drop increases, indicating an increasing ion diffusion resistance within the hierarchically

porous structure of the electrode.<sup>43</sup> The calculated specific capacitances as a function of current density are plotted in Fig. 8c. The specific capacitances are  $203 F g^{-1}$ ,  $209 F g^{-1}$  and  $70 F g^{-1}$  at  $5 mA cm^{-2}$  and retain  $157 F g^{-1}$ ,  $10 F g^{-1}$  and  $0 F g^{-1}$  at  $50 mA cm^{-2}$  for the samples activated at  $300 ^\circ C$ ,  $350 ^\circ C$  and  $400 ^\circ C$ , respectively. Generally, the electrochemical properties deteriorate with the increasing of activation temperature whatever from the point of view of energy density or the rate performance. Only at  $5 mA cm^{-2}$ , the specific capacitance of the sample activated at  $350 ^\circ C$  is highest owing to its highest microporosity.

Furthermore, EIS measurement is performed to study the charge conduction and ion diffusion behaviors through the electrode. The intercept of EIS spectra on  $Z'$  axis denotes the equivalent series resistance (ESR), including the resistance of electrode and electrolyte as well as the contact resistance between them. The diameter of semicircle in the high frequency region is controlled by the charge transfer resistance and the length of Warburg curve with a slope of  $45^\circ$  in the middle frequency region reflects the ion diffusion rate.<sup>44</sup> In low frequency region, a steeper line means a better capacitive

behavior. As shown in Fig. 8d, the ESR of these electrodes are approximate, but the charge transfer resistance and ion diffusion resistance both increased with the increase of activation temperature, which damage the rate capability. As mentioned above (Fig. 1b), the lack of surface acidic group (carboxyl and hydroxyl) leads to a weak interaction between the activated carbon surface and alkaline electrolyte, since surface acidic groups provide sites that can form exceptionally strong hydrogen bonds with weak acids and bases.<sup>21</sup> It appears surface active carboxyl/hydroxyl groups play a much more important role for determining the electrochemical performance, considering that the sample activated at 350 °C has the highest microporosity.

The effects of activation time are not as intense as the activation temperature, as seen from Fig. 9. The covered area by CV loop (Fig. 9a) and the IR drop shown in GCD curves (Fig. 9b) change insignificantly until the activation time increases to 3 h. The EIS spectra in Fig. 9c shows that all of the ESR resistance, the charge transfer resistance and the ion diffusion resistance increase with the prolonged activation time, especially for the sample activated for 3 h. The specific capacitances of all samples at various current density are shown in Fig. 9d. The capacitances at low current densities of 5 mA cm<sup>-2</sup> and 10 mA cm<sup>-2</sup> present an upward trend with the increase of activation time, but a downward trend at high current density range. Therefore, the activation time has a positive effect on the energy density, but a negative effect on the rate performance. On one hand, the enhanced specific surface area generated by air activation promote the energy density. On the other hand, the loss of surface acidic groups, caused by gradually intensive activation effect, results in the damage of the electrochemical performance of the electrode. Overall, the optimum condition is 300 °C of the activation temperature and 1 h of the activation time. Fig. 9e shows the GCD curves for the sample activated for 1 h at 300 °C from 5 mA cm<sup>-2</sup> to 50 mA cm<sup>-2</sup>. The capacitance increases 18% compared with the non-activation sample.<sup>29</sup> The cycle stability is tested at 50 mA cm<sup>-2</sup> for 10 000 cycles, as plotted in Fig. 9f. The average specific capacitance is 154 F g<sup>-1</sup> in the first 2000 cycles and rises to about 180 F g<sup>-1</sup> later. After 10 000 cycles, the electrode loses 4% (172 F g<sup>-1</sup>) of the capacitance, exhibiting an excellent cycling stability.

To obtain a comprehensive evaluation of the electrode, areal specific capacitance and total capacitance should be considered apart from the gravimetric specific capacitance.<sup>45,46</sup> Table 3 lists various capacitances of biomass-derived carbon electrode in pellet or monolith form as well as some polymer-derived monolithic carbon electrodes. The electrodes in pellet form possess a higher gravimetric specific capacitance (200–400 F g<sup>-1</sup>) than the monolithic electrodes (100–300 F g<sup>-1</sup>), due to their high specific surface area. However, the areal specific capacitance is only one-third of the capacitance of monolithic electrodes because of the limited accessible surface area by electrolyte in pellet electrodes. The introduced additives in the preparation of pellet electrodes hinder the infiltration of the electrolyte, which further lead to a limited mass loading of the active electrode materials. The total capacitance is thus at a level of <1 F cm<sup>-2</sup>. Owing to the hierarchically porous structure of

monolithic electrode, the total capacitance reaches to a value of >3 F cm<sup>-2</sup>. For the monolithic electrode, volumetric specific capacitance is another important indicator as the space for power device is usually limited.<sup>2</sup> The volumetric specific capacitance of the prepared electrodes in this work is comparable to other reported monolithic electrodes. Given that the air activation method excluding corrosive chemicals and complicated preparation process is mild and simple, the cotton rose-derived carbon electrodes outperform others.

## 4. Conclusion

Ultra-thick activated carbon monoliths, with a unique hierarchically porous structure and a high micro-porosity, have been prepared by air activation of charcoal, using cotton rose wood as raw materials. The properties of activated carbon monoliths are controlled by the activation temperature and time. Particular attention is paid to give an insight for the activation mechanism. It is demonstrated that the oxygen atoms are introduced by chemisorption and oxidation reactions and removed by dehydration and decomposition reactions through which the active carbon atoms on the surface are consumed layer by layer. Pores are thus produced on the surface of the charcoal channel. The results show that appropriate activation promotes the generating of micro-pores, but excessive activation leads the micropores to be meso-macropores and fast loss of acidic functional groups that are beneficial for absorbing electrolyte. The activated carbon monolith, activated at 300 °C for 1 h, shows the highest micro-porosity of 86% and a specific surface area of 567 m<sup>2</sup> g<sup>-1</sup>. The specific capacitance is 203 F g<sup>-1</sup> at 5 mA cm<sup>-2</sup> and still remains 157 F g<sup>-1</sup> at 50 mA cm<sup>-2</sup>, with 96% retention of its highest capacitance after 10 000 cycles at 50 mA cm<sup>-2</sup>. Furthermore, a comprehensive evaluation for the properties of electrodes shows that the as obtained activated carbon monolith outperforms other biomass-derived carbon materials considering the accessible available micro-porosity, total capacitance and green preparation method. These findings give a reference for preparing activated carbon monoliths using oxidizing gas for surface activation which is a green and sustainable technology.

## Conflicts of interest

There are no conflicts of interest to declare.

## Acknowledgements

This work was supported by National Key R&D Program of China (2017YFB0406200, 2018YFF01013605), Natural Science Foundation of China (No. 51902327), the Youth Innovation Promotion Association CAS (No. 2019254), Science Foundation for Youth Scholar of State Key Laboratory of High Performance Ceramics and Superfine Microstructures (SKL201701).

## References

- 1 P. Simon and Y. Gogotsi, *Nat. Mater.*, 2008, 7, 845–854.



- 2 K. Fic, A. Platek, J. Piwek and E. Frackowiak, *Mater. Today*, 2018, **21**, 437–454.
- 3 J. L. Huang, B. T. Zhao, T. Liu, J. R. Mou, Z. J. Jiang, J. Liu, H. X. Li and M. L. Liu, *Adv. Funct. Mater.*, 2019, **29**, 1902255.
- 4 M. Winter and R. J. Brodd, *Chem. Rev.*, 2004, **104**, 4245–4269.
- 5 J. R. Miller, *J. Power Sources*, 2016, **326**, 726–735.
- 6 D. Z. Wang, Y. Y. Xiao, X. N. Luo, Z. Z. Wu, Y. J. Wang and B. Fang, *ACS Sustainable Chem. Eng.*, 2017, **5**, 2509–2515.
- 7 B. Muthulakshmi, D. Kalpana, S. Pitchumani and N. G. Renganathan, *J. Power Sources*, 2006, **158**, 1533–1537.
- 8 J. Deng, M. M. Li and Y. Wang, *Green Chem.*, 2016, **18**, 4824–4854.
- 9 B. Fang, Y. Z. Wei and M. Kumagai, *J. Power Sources*, 2006, **155**, 487–491.
- 10 B. Fang, Y. Z. Wei, K. Suzuki and M. Kumagai, *Electrochim. Acta*, 2005, **50**, 3616–3621.
- 11 Y. L. Xing, B. Z. Fang, A. Bonakdarpour, S. C. Zhang and D. P. Wilkinson, *Int. J. Hydrogen Energy*, 2014, **39**, 7859–7867.
- 12 B. Fang, J. H. Kim, M. S. Kim and J. S. Yu, *Acc. Chem. Res.*, 2013, **46**, 1397–1406.
- 13 J. L. Yong, F. Chen, Q. Yang, J. L. Huo and X. Hou, *Chem. Soc. Rev.*, 2017, **46**, 4176–4190.
- 14 D. C. Martinez-Casillas, I. Mascorro-Gutierrez, C. E. Arreola-Ramos, H. I. Villafan-Vidales, C. A. Arancibia-Bulnes, V. H. Ramos-Sanchez and A. K. Cuentas-Gallegos, *Carbon*, 2019, **148**, 403–412.
- 15 H. Q. Gao, D. Zhang, H. T. Zhou, J. C. Wu, G. J. Xu, Z. L. Huang, M. H. Liu, J. H. Yang and D. Chen, *Appl. Surf. Sci.*, 2020, **534**, 147613.
- 16 C. J. Chen, Y. Zhang, Y. J. Li, J. Q. Dai, J. W. Song, Y. G. Yao, Y. H. Gong, I. Kierzewski, J. Xie and L. B. Hu, *Energy Environ. Sci.*, 2017, **10**, 538–545.
- 17 J. Marousek, O. Strunecy and V. Stehel, *Clean Technol. Environ.*, 2019, **21**, 1389–1395.
- 18 M. Danish and T. Ahmad, *Renewable Sustainable Energy Rev.*, 2018, **87**, 1–21.
- 19 K. Tomkow, A. Jankowska, F. Czechowski and T. Siemieniowska, *Fuel*, 1977, **56**, 101–106.
- 20 J. Yin, W. L. Zhang, N. A. Alhebshi, N. Salah and H. N. Alshareef, *Small Methods*, 2020, **4**, 1900853.
- 21 F. Xiao and J. J. Pignatello, *Environ. Sci. Technol.*, 2016, **50**, 6276–6283.
- 22 H. Q. Xuan, Y. L. Wang, G. X. Lin, F. Wang, L. Zhou, X. P. Dong and Z. Chen, *RSC Adv.*, 2016, **6**, 15313–15319.
- 23 E. M. Lotfabad, J. Ding, K. Cui, A. Kohandehghan, W. P. Kalisvaart, M. Hazelton and D. Mitlin, *ACS Nano*, 2014, **8**, 7115–7129.
- 24 R. Bardestani and S. Kaliaguine, *Biomass Bioenergy*, 2018, **108**, 101–112.
- 25 Z. Li, L. Zhang, B. S. Amirkhiz, X. H. Tan, Z. W. Xu, H. L. Wang, B. C. Olsen, C. M. B. Holt and D. Mitlin, *Adv. Energy Mater.*, 2012, **2**, 431–437.
- 26 W. J. Zhang, T. Liu, J. R. Mou, J. L. Huang and M. L. Liu, *Phys. Chem. Chem. Phys.*, 2020, **22**, 2073–2080.
- 27 Y. Ma, D. X. Yao, H. Q. Liang, J. W. Yin, Y. F. Xia, K. H. Zuo and Y. P. Zeng, *Electrochim. Acta*, 2020, **352**, 136452.
- 28 M. Sevilla, G. A. Ferrero and A. B. Fuertes, *Carbon*, 2017, **114**, 50–58.
- 29 Y. Ma, Y. S. Li and Y. P. Zeng, *J. Mater. Sci.*, 2021, **56**, 8588–8599.
- 30 S. Biniak, G. Szymanski, J. Siedlewski and A. Swiatkowski, *Carbon*, 1997, **35**, 1799–1810.
- 31 A. C. Lua and T. Yang, *J. Colloid Interface Sci.*, 2004, **276**, 364–372.
- 32 C. Moreno-Castilla, M. V. Lopez-Ramon and F. Carrasco-Marin, *Carbon*, 2000, **38**, 1995–2001.
- 33 J. L. Figueiredo, M. F. R. Pereira, M. M. A. Freitas and J. J. M. Orfao, *Carbon*, 1999, **37**, 1379–1389.
- 34 H. Deng, G. X. Li, H. B. Yang, J. P. Tang and J. Y. Tang, *Chem. Eng. J.*, 2010, **163**, 373–381.
- 35 K. Wang, N. Zhao, S. W. Lei, R. Yan, X. D. Tian, J. Z. Wang, Y. Song, D. F. Xu, Q. G. Guo and L. Liu, *Electrochim. Acta*, 2015, **166**, 1–11.
- 36 S. J. Song, F. W. Ma, G. Wu, D. Ma, W. D. Geng and J. F. Wan, *J. Mater. Chem. A*, 2015, **3**, 18154–18162.
- 37 A. F. Perez-Cadenas, F. J. Maldonado-Hodar and C. Moreno-Castilla, *Carbon*, 2003, **41**, 473–478.
- 38 S. Liu, J. Q. Tian, L. Wang, Y. W. Zhang, X. Y. Qin, Y. L. Luo, A. M. Asiri, A. O. Al-Youbi and X. P. Sun, *Adv. Mater.*, 2012, **24**, 2037–2041.
- 39 G. delaPuente, J. J. Pis, J. A. Menendez and P. Grange, *J. Anal. Appl. Pyrolysis*, 1997, **43**, 125–138.
- 40 F. Xiao, A. H. Bedane, J. L. X. J. Zhao, M. D. Mann and J. J. Pignatello, *Sci. Total Environ.*, 2018, **618**, 276–283.
- 41 Z. F. Yu, X. Z. Wang, X. D. Song, Y. Liu and J. S. Qiu, *Carbon*, 2015, **95**, 852–860.
- 42 X. Deng, B. T. Zhao, L. Zhu and Z. P. Shao, *Carbon*, 2015, **93**, 48–58.
- 43 P. Cheng, S. Y. Gao, P. Y. Zang, X. F. Yang, Y. L. Bai, H. Xu, Z. H. Liu and Z. B. Lei, *Carbon*, 2015, **93**, 315–324.
- 44 Y. X. Xu, Z. Y. Lin, X. Zhong, X. Q. Huang, N. O. Weiss, Y. Huang and X. F. Duan, *Nat. Commun.*, 2014, **5**, 4554.
- 45 H. Li, D. Yuan, C. H. Tang, S. X. Wang, J. T. Sun, Z. B. Li, T. Tang, F. K. Wang, H. Gong and C. B. He, *Carbon*, 2016, **100**, 151–157.
- 46 J. Pang, W. F. Zhang, J. L. Zhang, G. P. Cao, M. F. Han and Y. S. Yang, *Green Chem.*, 2017, **19**, 3916–3926.
- 47 Y. N. Gong, D. L. Li, C. Z. Luo, Q. Fu and C. X. Pan, *Green Chem.*, 2017, **19**, 4132–4140.
- 48 J. M. Li, Q. M. Jiang, L. S. Wei, L. X. Zhong and X. Y. Wang, *J. Mater. Chem. A*, 2020, **8**, 1469–1479.
- 49 R. T. Wang, P. Y. Wang, X. B. Yan, J. W. Lang, C. Peng and Q. J. Xue, *ACS Appl. Mater. Interfaces*, 2012, **4**, 5800–5806.
- 50 J. Wu, M. W. Xia, X. Zhang, Y. Q. Chen, F. Sun, X. H. Wang, H. P. Yang and H. P. Chen, *J. Power Sources*, 2020, **455**, 227982.
- 51 G. Qu, S. F. Jia, H. Wang, F. Cao, L. Li, C. Qing, D. M. Sun, B. X. Wang, Y. W. Tang and J. B. Wang, *ACS Appl. Mater. Interfaces*, 2016, **8**, 20822–20830.
- 52 L. Wang, G. Mu, C. G. Tian, L. Sun, W. Zhou, P. Yu, J. Yin and H. G. Fu, *ChemSusChem*, 2013, **6**, 880–889.
- 53 C. Peng, X. B. Yan, R. T. Wang, J. W. Lang, Y. J. Ou and Q. J. Xue, *Electrochim. Acta*, 2013, **87**, 401–408.

- 54 L. Sun, C. G. Tian, M. T. Li, X. Y. Meng, L. Wang, R. H. Wang, J. Yin and H. G. Fu, *J. Mater. Chem. A*, 2013, **1**, 6462–6470.
- 55 M. C. Liu, L. B. Kong, P. Zhang, Y. C. Luo and L. Kang, *Electrochim. Acta*, 2012, **60**, 443–448.
- 56 J. H. Jiang, L. Zhang, X. Y. Wang, N. Holm, K. Rajagopalan, F. L. Chen and S. G. Ma, *Electrochim. Acta*, 2013, **113**, 481–489.
- 57 S. Zhang, C. L. Wu, W. Wu, C. Zhou, Z. W. Xi, Y. Y. Deng, X. Wang, P. Quan, X. J. Li and Y. F. Luo, *J. Power Sources*, 2019, **424**, 1–7.
- 58 Y. R. Liu, *J. Porous Mater.*, 2014, **21**, 1009–1014.
- 59 Y. F. Yu, J. Du, L. Liu, G. X. Wang, H. L. Zhang and A. B. Chen, *J. Nanopart. Res.*, 2017, **19**, 119.